The Aeronautical Journal (2025), 1–21
doi:10.1017/aer.2025.10060

ROYAL AERONAUTICAL SOCIETY

RESEARCH ARTICLE

Aeroelastic analysis of propeller blades at stall flutter onset

M. McKechnie and G. Barakos

CFD Laboratory, School of Engineering, University of Glasgow, Glasgow, G12 8QQ, UK
Corresponding author: G. Barakos; Email: george.barakos@glasgow.ac.uk

Received: 21 November 2024; **Revised:** 22 July 2025; **Accepted:** 22 July 2025

Keywords: fluid structure interaction; propellers; flutter

Abstract

Aeroelastic analyses are part of the design of modern propeller blades. Most of the time, advanced numerical simulations are used, involving computational fluid dynamics. However, the coupling between fluid and structure may be missing. In this paper, two coupled fluid-structure interaction methods are presented, namely the modal time-marching and the quasi-static approach. An in-house aeroelastic tool, analysing an in-house blade design, is used. A limited number of experiments are available, and this was alleviated using new experiments as part of the Numerical and Experimental Study of Propeller Aeroelasticity project. In this work, 3D finite element models (FEM) were used to represent the blade structure. Time-marching and quasi-steady results were compared, and this is the first time that this is reported in the literature. It was found that regardless of the differences in the aerodynamic loads between time-marching and quasi-static computations, the final blade deformations were comparable. Time-marching computations using a modal representation of the blade, obtained from 3D FEM, showed that the blade deformation and vibration were driven by the stalled flow. This observation was verified by comparing the blade response with the flow off-the-blade. The harmonic content of the results includes the propeller blade passing frequency and its natural frequencies, but also additional frequencies related to the flow shedding and vortical content of the stalled part of the blade. To the best of our knowledge, this has not been reported in the open literature.

Nomenclature

Latin

D	diameter
$f_m^s(t)$	modal forces
i, j, k	indices
J	advance ratio
k	number of neighbouring points
$\mathbf{M}$	mass matrix
m_j	generalised mass
n	rotational frequency
N	number of inner time steps
nx	number of points in x
ny	number of points in y
nz	number of points in z
p	pressure
$\mathbf{p}$	a given point
$\mathbb{P}$	power parameter
R	residual vector
$\mathbf{R}$	radius
s	solid (blade)
t	real-time step or time
V	axial velocity

https://doi.org/10.1017/aer.2025.10060 Published online by Cambridge University Press

W	vector of conserved variables
w_i	interpolation weights

Greek

α_m^s	modal amplitude
ζ_m	structural damping coefficient
η_m	mode shape of the m^{th} mode
τ	pseudo time step
$\phi_m^s\ (p)$	supplied mode shapes
$\phi^s\ (t)$	deformed blade shape at time t
ϕ_0^s	rigid shape
ω_m	modal frequency

Acronyms

ADT	alternating digital tree
BILU	block incomplete lower-upper
BLADE	Bristol Laboratory for Advanced Dynamic Engineering
CFD	computational fluid dynamics
CSD	computational structural dynamics
eVTOL	electric vertical take off and landing
FE	finite element
FEM	finite element method
HMB3	helicopter multi block 3
IDW	inverse distance weighting
IMPACTA	improving the propulsion aerodynamics and acoustics of turboprop aircraft
JORP	joint open rotor program
MENtOR	methods and experiments for novel rotorcraft
MLS	moving least squares
MUSCL	Monotone Upstream-Centred Scheme for Conservation Laws
NASTRAN	NASA structural analysis
RANS/URANS	unsteady/ Reynolds-averaged Navier-Stokes
SOL	NASTRAN solution
SR	single rotation
SST	shear stress transport

1.0 Introduction

Stall flutter is defined as the oscillation of a body due to the partial or full separation of the flowfield around it [1]. Propeller blades have operating conditions, within their flight envelop, that can lead to stall. Where the blades have relatively high rotational rates with low axial velocity, i.e. low advance ratio, $J = \frac{V}{nD}$, (where V is the axial velocity, n is the rotational frequency and D is the propeller diameter). Furthermore, blade stall characteristics also depend on the blade pitch angle. Stall conditions can occur on the runway, during take-off of turbo-prop aircraft, or they may appear in new electric vertical take off and landing (eVTOL) or tilt rotor aircraft in the transition stages from hover to forward flight. There is also a constant demand for better-performing, quieter blades, which often means thinner blade sections. Other design characteristics, such as larger twist, swept tip sections, and tip anhedral, can make the blades more susceptible to stall. Higgins [2], shown that stall flutter is driven by the design, but the non-linear, stalled aerodynamics, means that the flutter boundary of stall flutter is significantly reduced in comparison with bending-torsion flutter. Aside from the work by Higgins, there are no other high-fidelity numerical propeller stall flutter studies. Delamore-Sutcliffe [3] developed a low-order model based on an eigenvalue solution, which assesses blade stability. This model was validated using the experimental data

https://doi.org/10.1017/aer.2025.10060 Published online by Cambridge University Press

of Baker [4]. However, the model assumptions limit its capabilities for application in modern propeller designs. There are very few experimental stall flutter studies, and even if data exists, these often come from accidental occurrences of flutter during performance testing, which led to the test runs being shut down [5]. One of the most comprehensive sets of blade flutter experiments was conducted by NASA on the single rotation (SR) blades [6–8] between 1970 and 1990. Blade deformations, both static and dynamic, were tested during an extensive campaign, which concluded that classical flutter is sufficiently understood; therefore, propellers can be designed to avoid this [9]. However, the aerodynamic non-linearity of stall flutter is a much more challenging concept. Dowty Rotol also reported an experimental test campaign where initial testing had to be cancelled due to concerning amounts of noise from strain gauges indicating flutter [10]. In recent years, experimental tests for the methods and experiments for NOvel Rotorcraft (MENtOR) propeller blade have been conducted on the UK National Rotor Rig [11]. These campaigns have also considered the onset of stall on these blades [12] and in further work to explore the frequencies from the strain gauges and compare with the modal frequencies of the propeller blades in stalled flow [13]. The novelty of the work is that 3D finite elements (FE) are used for the structural representation of the blade, and this is combined with numerical analyses compared with the limited available experimental data. Dynamic fluid/structure interaction computations were used for the study of stall flutter, and it was evident that the frequency content of the blade response was driven by both its natural modes of oscillation and the frequency content of the stalled part of the flow. This was confirmed by on-the-blade and off-the-blade comparisons of the simulation results in terms of their frequency content and associated amplitudes. This work is a positive step in the increase of fidelity of the simulations of stall flutter and puts forward a method that is of high fidelity in comparison to the use of beam-based models or simplified stalled-flow aerodynamic models.

2.0 Simulation methodology

2.1 Methodology of the study

To minimise our computational resources, simulation cases were first conducted using the static aeroelastic method with steady flow assumptions. The results of these cases would indicate if the flow was attached or separated. These calculations were of very low cost compared to the dynamic aeroelastic methods, and hence if the flow was displaying periodic behaviour then only the static aeroelastic methods are required. However, if the flow displays separated regions with aperiodic loading then the dynamic aeroelasticity methods are required. The blade pitch angles and rotational speeds were set to match the experimental cases, validation data was obtained for the static aeroelastic cases. Then the numerical work could explore more conditions that could not be achieved experimentally as well as a conceptually softened blade.

2.2 CFD solver

This work uses the Helicopter Multi-Block 3 (HMB3) computational fluid dynamic (CFD) solver that has been developed for rotorcraft flows and helicopter blade design [14, 15]. However, HMB3 has also been used for propeller cases. These were mainly validation cases in both installed and isolated flight conditions [16, 17], using data from experimental campaigns such as the joint open rotor program (JORP) [18], and the improving the propulsion aerodynamics and acoustics of turboprop aircraft (IMPACTA) propellers [19, 20]. Comparisons with experimental inflow investigations at the University of Glasgow for model propeller blades in axial flight and at yaw [21] have also been conducted.

In HMB3, the Navier-Stokes equations are solved using the cell-centred, finite volume approach on multi-block grids. The unsteady/ Reynolds-averaged Navier-Stokes (RANS/URANS) system of ordinary differential equations after discretisation are:

$$\frac{dW}{dt} + \frac{dW}{d\tau} + R(W) = 0, \tag{1}$$

https://doi.org/10.1017/aer.2025.10060 Published online by Cambridge University Press

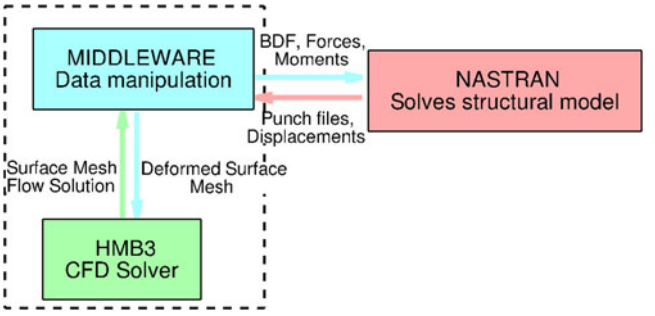

Figure 1. *Using the middleware to couple HMB3 to MSC/NASTRAN.*

where, W is the vector of conserved variables, R is the residual vector, t is the real time step and τ is the pseudo time step, of a dual-time stepping method. The steady state discretisation is the same other than the pseudo time step term, $\left(\frac{dW}{d\tau}\right)$, is removed.

The convective fluxes are evaluated using Osher's approximate Riemann solver [22], and the viscous terms with second-order central differences in space. To provide high-order accuracy in space, the Monotone Upstream-centred Scheme for Conservation Laws (MUSCL) with the developments of Leer [23] is employed.

For steady-state calculations, a non-inertial reference frame is used. Therefore, a source term and mesh velocities are added to account for the centripetal and Coriolis accelerations [14]. For the unsteady time-marching method, the temporal integration is performed with the implicit dual-time stepping technique of Jameson [24]. For each time step there is a pseudo-time τ where the solution is marched to steady state. The linearised system is then solved with the generalised conjugate gradient (CG) method with a block incomplete lower-upper (BILU) factorisation [25].

2.3 Fluid structure interaction

2.3.1 Static aeroelasticity

An in-house computer code coined 'Middleware' is used. Middleware is a communications utility within the HMB3 toolset. This facilitates data exchanges and data reformatting between the CFD solver and the structural solver (MSC-NASTRAN). The tool takes a CFD flow solution, passes forces and moments to the structural model, and then converts the deformed structure back onto the CFD mesh. This is an iterative process between the fluid and structural domains until the deformations converge. This iterative process is termed loose coupling and is applicable to cased where a periodic or steady state solution is sought. The process is demonstrated in Fig. 1. The converged flow solution for a rigid structure and its surface mesh is passed to Middleware. Middleware takes that flow solution and calculates the aerodynamic loads according to the structural model, e.g., the required MSC-NASTRAN force input will vary depending if a beam or 3D FE model is to be used. When this file is generated, MSC-NASTRAN is started and the deformation is calculated. For rotating blades the centrifugal effects are accounted for in the structural model. This is done using the MSC-NASTRAN RFORCE terms. After the structural deformation is calculated, Middleware post-processes the deformation and interpolates the deformation onto the CFD surface mesh. A set of grid points are generated on the aerodynamic surface of the blade. These points have a similar resolution to that of the finite element method (FEM) mesh. Each of these points is then connected to the nearest FEM grid point with a rigid bar element. This helps because it is easier to have a well-defined set of points that represent the deformed surface and can be used for the interpolation of the mesh deformation. When the FEM mesh deforms, the rigid bars also translate and rotate their corresponding mesh points to represent the deformed structural shape. Middleware then passes this deformed surface mesh back to HMB3 where the deformed volume mesh is calculated, and the CFD simulation continues with the now deformed mesh. This deformation causes a change

https://doi.org/10.1017/aer.2025.10060 Published online by Cambridge University Press

in the aerodynamic loads, which is why it is an iterative process between fluid and structure through Middleware.

The mesh deformation procedure is the same for the static (middleware) and the dynamic aeroelastic method (modal method). This is discussed in section 2.3.2.

2.3.2 Dynamic aeroelasticity

The dynamic aeroelasticity method of HMB3 is based on the modal method [26]. This is used here for stalled flow cases with dynamic fluid-structure interaction. However, it could also be used for static cases. This is not done because it would require unnecessary expense over our Middleware method. The method uses structural modes and frequencies from a modal FE or beam solution, and projects the forces to the mode shapes. From this, deformations can be obtained for each of the structural modes. Like Middleware, the mesh deformation procedure is based on the inverse distance weighting interpolation and is described in section 2.3.4.

The same finite element model that is used for Middleware calculations is also used with the modal method. Here the NASTRAN model is used to obtain the structural mode shapes and frequencies. The structural model itself is a full FEM, it has interface connection between each of the parts, and the material properties are supplied to each part. For non-matching connections (termed 'glue' connections in MSC-NASTRAN), eigenmode result requirements and structural solver limitations, an implicit nonlinear solution method is used (SOL400). This solver allows loads to be applied, glue connections and an eigen analysis in a singular calculation. In our case, the load is centrifugal load and including this in the eigenmode calculation accounts for rotational stiffening. It is essential that the employed unit system matches that of the CFD simulation. This is because the mode shapes are mass scaled, and each displacement vector is divided by the generalised mass. The representative length of each of these vectors is crucial for the modal force calculation to be correct.

Before the CFD calculation begins, the CFD solver takes the supplied mode shapes and interpolates each of the eigenmodes onto the CFD mesh, this is conducted using the MLS method. The CSD to CFD mesh interpolation only needs to be done at the start of the simulation and then the interpolated eigenmode deformed shapes for the CFD mesh can be used throughout the rest of the simulation for every time step. Also, the transfer of the aerodynamic loads to the structure can be applied directly to these deformed CFD mesh shapes rather than requiring further interpolation.

2.3.3 Computation of modal loads and amplitudes

At each time step, the pressure p of the CFD solution is integrated over the undeformed mesh points to compute the modal forces $f_m^s\,(t)$ on the blade (s). This is done for each of the supplied mode shapes $\phi_m^s\,(p)$. The following holds:

$$f_m^s(t) = \sum_{p=1}^{n_s} \mathbf{p}(p,t).\phi_m^s(p), \tag{2}$$

where, n_s is the number of CFD mesh points on the blade, $\mathbf{p}\,(p,t)$ describes the pressure at point $\mathbf{p}$ and $\phi_m^s\,(p)$ is the modal shape at point p for the m^{th} mode of the blade (s). To resolve the mode shape correctly, mode scaling is critical. The mode shapes are scaled in MSC-NASTRAN with a generalised mass (m_j) of 1 kg. Therefore, the modal forces have units of $N/m.kg$. The mode shapes are:

$$m_m = {\eta_m}^T[\mathbf{M}]\eta_m, \tag{3}$$

Here, η_m is the mode shape of the m^{th} mode, and $\mathbf{M}$ is the mass matrix [27]. The deformed shape is computed from:

$$\phi^s(t) = \phi_0^s + \sum_{m=1}^{n_m^s} \alpha_m^s(t)\phi_m^s, \tag{4}$$

https://doi.org/10.1017/aer.2025.10060 Published online by Cambridge University Press

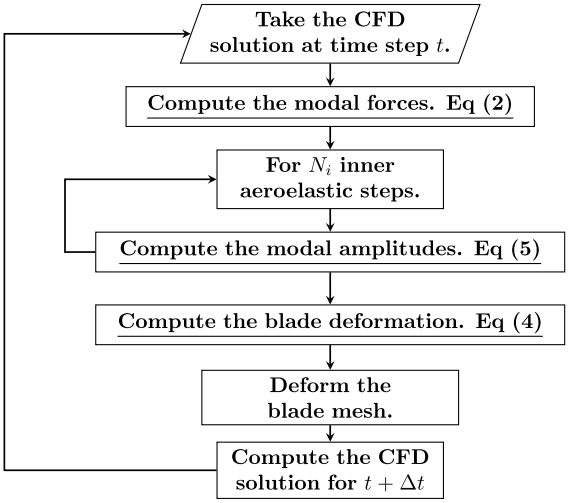

Figure 2. *Modal method process.*

as the sum of the rigid shape ϕ_0^s plus the sum of the modal amplitudes $\alpha_m^s(t)$ multiplied by their corresponding mode shapes ϕ_m^s. The modal amplitudes are computed using:

$$\frac{\partial^2 \alpha_m^s}{\partial t^2} + 2\zeta_m \omega_m \frac{\partial \alpha_m^s}{\partial t} + \omega_m^2 \alpha_m^s = f_m^s(t). \tag{5}$$

Here, ζ_m is the structural damping coefficient, ω_m is the modal frequency and $f_m^s(t)$ is the modal forcing term of Equation (2).

At the start of each calculation, a large damping coefficient is used, typically $\zeta_m = 0.3$. The aim here is to get the blade to deform to an approximate averaged deformed position; this approximates the static aeroelastic deformation. The value needs to be sufficient enough to avoid a drastic instability and diverge during the early steps of the simulation. After that, the damping is reduced to $\zeta_m = 0.01$, which is based on previous studies [2].

The leap-frog method [28, 29] is used to solve Equation (5). To ensure stability of higher-order modes, each time step is solved with N inner time steps of size $\Delta t_i = \Delta t/N$ (where i is the counter to N). The modal force at the time $t_i = t + i\Delta t_i$ is :

$$f_m^s(t_i) = f_m^s(t) + \frac{i\left(f_m^s(t+\Delta t) - f_m^s(t)\right)}{N} \tag{6}$$

The m-th amplitude α_m^s is then assessed for inner time-step t_{i+1}:

$$\left[\alpha_m^s\right]_{t_{i+1}} = \left[\alpha_m^s\right]_{t_i} + \left[\frac{\partial \alpha_m^s}{\partial t_i}\right]_{t_i} \Delta t_i + \frac{1}{2}\left[\frac{\partial^2 \alpha_m^s}{\partial t_i^2}\right]_{t_i} \Delta t_i^2 \tag{7}$$

Then the time derivative of the amplitudes is then computed as:

$$\begin{aligned}
\left[\frac{\partial^2 \alpha_m^s}{\partial t_i^2}\right]_{t_{i+1}} &= \left[f_m^s\right]_{t_i} - \omega_m^2 \left[\alpha_m^s\right]_{t_i} - 2\zeta\omega_m \left[\frac{\partial \alpha_m^s}{\partial t_i}\right]_{t_i} \\
\left[\frac{\partial \alpha_m^s}{\partial t_i}\right]_{t_{i+1}} &= \left[\frac{\partial \alpha_m^s}{\partial t_i}\right]_{t_i} + \frac{1}{2}\left(\left[\frac{\partial^2 \alpha_m}{\partial t_i^2}\right]_{t_i} + \left[\frac{\partial^2 \alpha_m^s}{\partial t_i^2}\right]_{t_{i+1}}\right) \Delta t_i
\end{aligned} \tag{8}$$

This method has been summarised in Fig. 2.

https://doi.org/10.1017/aer.2025.10060 Published online by Cambridge University Press

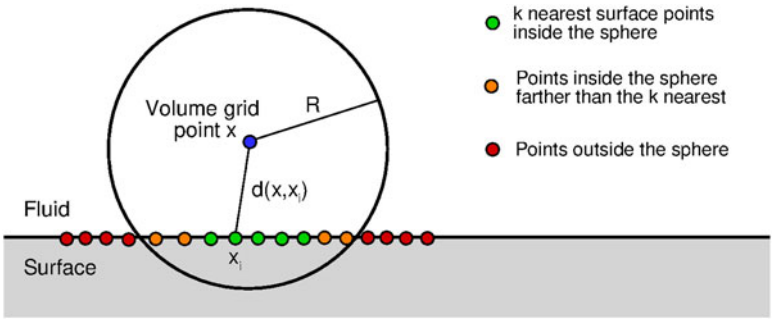

Figure 3. *Illustration of the point selection process in order to compute the IDW weights.*

2.3.4 Deformation of the volume mesh

After the surface mesh is deformed with the moving least squares method (MLS), the volume mesh is then deformed to that surface with the inverse distance weighting (IDW) method [30]. This method was incorporated into HMB3 directly. The IDW method interpolates values at an unknown point by taking the weighted average of a known set of neighbouring points. The weighting factor given to a known point is proportional to the inverse distance between the known and unknown points. Biava et al. [31] have shown that even after mesh deformation, the mesh was still of high quality.

Given N samples $\mathbf{u}_i = u(\mathbf{x}_i)$ for $i = 1, 2, \ldots, N$, the IDW interpolated value of the function $\mathbf{u}$ at a point $\mathbf{x}$ is:

$$\mathbf{u}(\mathbf{x}) = \begin{cases} \dfrac{\sum_{i=1}^{N} w_i(\mathbf{x})\mathbf{u_i}}{\sum_{i=1}^{N} w_i(\mathbf{x})}, & \text{if } d(\mathbf{x}, \mathbf{x_i}) \neq \mathbf{0} \text{ for all } \mathbf{i} \\ \mathbf{u_i}, & \text{if } d(\mathbf{x}, \mathbf{x_i}) = \mathbf{0} \text{ for some } \mathbf{i} \end{cases}, \tag{9}$$

where

$$w_i(\mathbf{x}) = \frac{\mathbf{1}}{\mathbf{d}(\mathbf{x}, \mathbf{x_i})^{\mathbb{P}}} \tag{10}$$

In these equations, $\mathbb{P}$ is the power parameter that can be any positive real number, and $d((\mathbf{x}), (\mathbf{y}))$ is the Euclidean distance between $(\mathbf{x})$ and $(\mathbf{y})$.

With larger meshes, the original form of the IDW method scales linearly and becomes more expensive. Therefore, Renka's method [32] is a reduction of the formulation where a sphere is considered for each volumetric grid point of radius $\mathbf{R}$ and only considers k nearest neighbours. This is shown in Fig. 3. The interpolation weights are:

$$w_i(\mathbf{x}) = \left(\frac{\max(\mathbf{0}, \mathbf{R} - \mathbf{d}(\mathbf{x}, \mathbf{x_i}))}{\mathbf{R}\mathbf{d}(\mathbf{x}, \mathbf{x_i})} \right)^{\mathbf{2}}, \quad \mathbf{i} = \mathbf{1}, \mathbf{2}, \ldots, \mathbf{k}. \tag{11}$$

The efficiency of this method depends on the efficiency of the spatial search of each of the spheres to find k nearest points. For this, an alternating digital tree (ADT) structure is used. Alongside this, a blending function is used to help smooth the mesh deformations after the interpolation. This means that the interpolated displacement tends to zero as the distance from the surface approaches $\mathbf{R}$.

2.4 CFD mesh

The CFD mesh utilises the Chimera method with bodyfitted, structured, multi-block mesh. For this, we have a background domain and a blade domain which can be observed in Figs 4a and 4(b)-(d) respectively. The background mesh has 11.5M cells, and the blade mesh has 6.6M cells, resulting in 18.1M

https://doi.org/10.1017/aer.2025.10060 Published online by Cambridge University Press

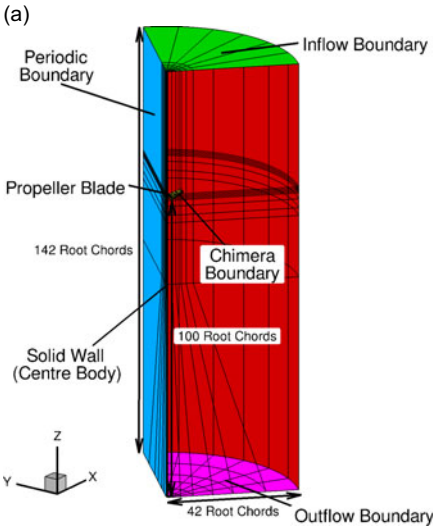

MENtOR background CFD mesh.

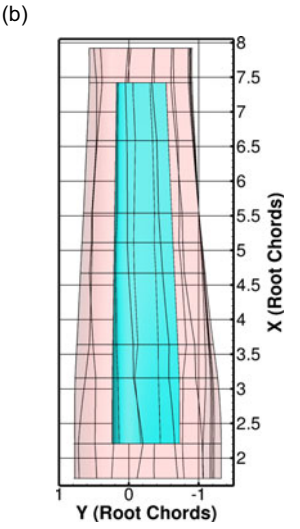

Propeller blade domain, XY plane.

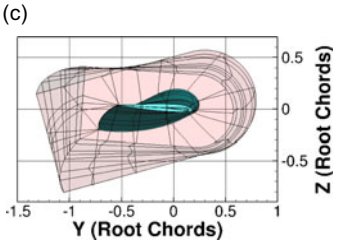

Propeller blade domain, YZ plane.

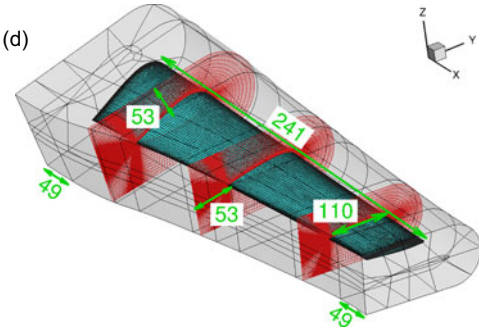

Propeller blade mesh, number of cells in each direction displayed.

Figure 4. *MENtOR background and blade CFD mesh.*

cells in the overall mesh. For the blade mesh, the chimera boundary extends 0.5 local sectional chord lengths off surface, with a wall distance of 10^{-5} root chords. There is a centre-body in the background mesh, which is a perfect cylinder running the entire length of the domain and has a radius of 0.5 root chords. The inflow, outflow boundaries and the outer cylindrical surfaces (shown in green, pink and red in Fig. 4(a)) have far-field conditions.

2.5 The MENtOR propeller blade

The MENtOR blade used for this project is of a similar design to an eVTOL tiltrotor blade. It uses three aerofoils: the NACA 64-128 at the root, the Vertol V23010_1.58 at 60%R and the Vertol V43015_2_48 at the blade tip. The twist and chord distribution can be seen in Fig. 5 (a). The blade is composed of six main parts: blade skin, tip cap, spar, rear filler, spar filler and the root fitting. The blade sections can be observed in Fig. 5(b), and the materials used are listed in Table 1. The propeller is composed of four blades, each with a radius of 625mm and a mass of 290.3g.

2.6 Finite element models

The finite element model consists of 1.9M tetrahedral elements and is shown in Fig. 6. For static aeroelastic analyses, the linear static SOL101 solver of MSC-NASTRAN is used. The aerodynamic loads are

https://doi.org/10.1017/aer.2025.10060 Published online by Cambridge University Press

Table 1. *MENtOR Blade, parts and materials*

Part	Material
Skin	Carbon fibre, [(0/90)/(+45/−45)/(+45/−45)/(0/90)]
Tip cap	Carbon fibre, [(0/90)/(+45/−45)/(+45/−45)/(0/90)]
Spar	Carbon fibre, [(0/90)/(0/90)/(0/90)/(0/90)]
Rear filler	ROHACELL 71HERO
Spar filler	ROHACELL 71HERO
Root fitting	AA7075-T651

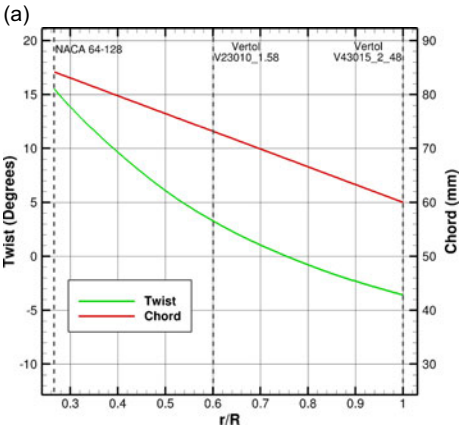

MENtOR propeller blade, sections, twist and chord.

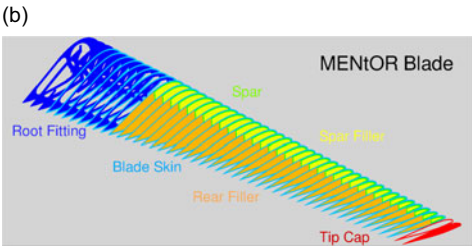

MENtOR blade parts.

Figure 5. *MENtOR background and blade CFD mesh.*

precomputed and formatted for MSC-NASTRAN, and the centrifugal force is applied using the MSC-NASTRAN RFORCE command. For dynamic aeroelastic analyses, the implicit, nonlinear, SOL400 method is used. This allows for an eigenmode analysis using non-matching interfaces (also known as 'glue' boundaries) between mesh parts.

A physical tap test using free-free conditions was conducted by the Bristol Laboratory for Advanced Dynamic Engineering (BLADE), and was also replicated numerically. The frequency comparison can be seen in Table 2, and the mode shape comparison in Fig. 7. This validates the FE model, before simulating the blades on the propeller rig. The use of the centrifugal term in the eigenmode analysis accounts for the centrifugal stiffening for the combined CFD/CSD simulation.

Tap tests were conducted at Bristol University, as part of the MENtOR project [33].

3.0 Results and discussion

3.1 Static aeroelasticity

Computations with steady flow assumptions were first conducted, and the blade torque was compared with wind tunnel data. These are presented in Figs 8 and 9, for pitch angles, 16, 25.5 and 35.7 degrees at the 75% radial section, 1080 revolutions per minute and at advance ratios from 0.08 to 1.3. The advance ratios were restricted by what was achievable in the wind tunnel, between power limits and reversed blade thrust. Figure 8 compares the numerical thrust and torque to experimental values. It can be observed that the simulation resolved the torque quite well. The comparisons suffer at the lower advance ratio and high collective pitch due to the steady, periodic flow assumptions used for this analysis. It can be observed in that the numerical torque is slightly less than the experimental torque for all advance ratios.

https://doi.org/10.1017/aer.2025.10060 Published online by Cambridge University Press

Table 2. *Free-free structural frequency comparisons and numerical, fixed root, modal frequencies for the baseline blade and the softened blade*

Mode	Experimental Frequency (Hz)	NASTRAN Free-Free (Hz)	NASTRAN Fixed Root, 3000 RPM (Hz)	NASTRAN, 50% Youngs' Modulus Blade, Fixed Root, 3000RPM, (Hz)
1	257.7–261.3	261.3	138.3	112.3
2	733.6–743.2	750.9	400.3	292.8
3	916.3–934.4	1055.9	529.9	386.8
4	1270.0–1301.9	1319.0	959.9	684.9
5	1397.1–1412.4	1421.6	987.1	713.6
6	–	2015.5	1563.8	1125.1
7	–	2073.8	1938.2	1377.8
8	–	2452.4	1982.2	1407.6
9	–	2682.4	2167.0	1554.4
10	–	2904.6	2518.1	1797.8

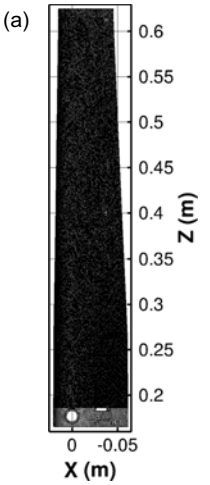

Overall view of the FE mesh.

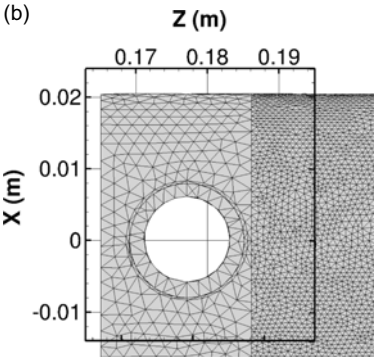

Detailed FE mesh view at the blade pin attachment.

Figure 6. *FEM mesh views.*

However, this is expected due to the numerical simulation only containing the blade with no spinner or rig present.

The displacements induced from the aerodynamic forces and moments are presented in Fig. 9. As expected, the tip quarter chord deformation plot follows the same trend as the loads. However, the lower advance ratio (stalled cases) suffered with the the steady flow assumption and require unsteady modelling. The results show how stiff the blades are, with the maximum recorded displacement approaching 2.4 mm, and the maximum change in pitch angle at the tip reaching -0.025 degrees. Here, negative results indicate pitch down deformations.

3.2 Dynamic aeroelasticity

Due to the limitations of the steady flow assumptions, the modal method was then used. These cases were for advance ratios of 0.3, 3000 revolutions per minute and the pitch angles of 32, 35.6 (baseline

https://doi.org/10.1017/aer.2025.10060 Published online by Cambridge University Press

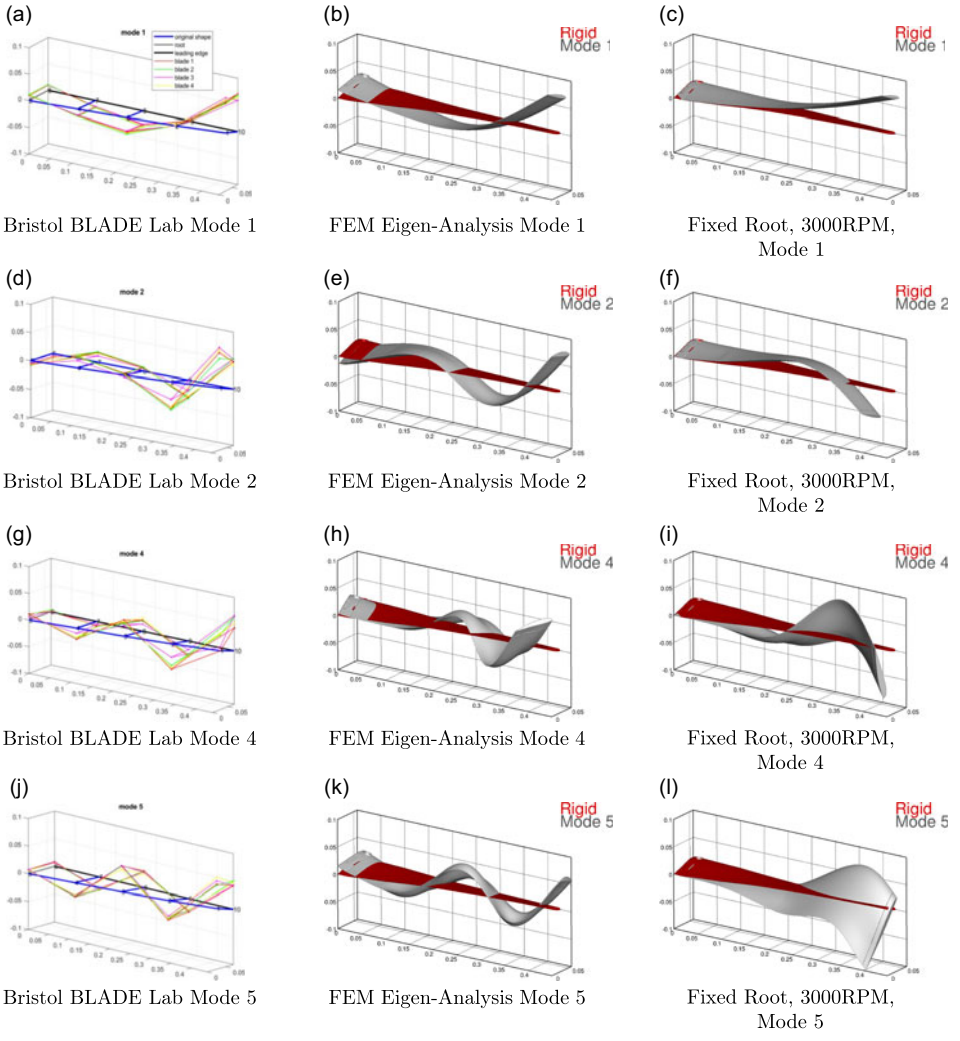

Figure 7. *Mode shape comparison between tap test and FEM, and fixed root, 3000RPM results.*

blade and softer blade) and 40.0 degrees at the 75% radial section. The flow around the blades can be seen in Fig. 10.

The modal amplitudes can be observed in Fig. 11; the largest deformations were associated with the first mode, which is the first bending mode. This was expected as it had the lowest frequency, and the modal force projection varied by a small factor. The mode shape for the first bending mode bends against the thrust direction, hence the amplitude is negative. This is the main contribution towards the aeroelastic coning of the blade. It can be clearly observed that the softer blade cones twice as much than the baseline blade. This increase was expected given the lower eigen-frequencies of the softer blade. Mode 2 displacements are approximately the same for all cases. For the baseline blade, the oscillations grow as the flow becomes more stalled. The oscillations are significantly larger for the softer blade as expected. Mode 4 is the first torsional mode. Three pitch angles for the baseline blades show that the modal amplitudes operate within a band and are of small magnitude. The softer blade results show increasing amplitude, indicating torsional divergence of this mode. We see similar results for mode 5 (second torsional mode) for the baseline blades and larger modal amplitudes of the softer blade, but these do not diverge like mode 4. Due to the stalled nature of these flows, the amplitudes are aperiodic

https://doi.org/10.1017/aer.2025.10060 Published online by Cambridge University Press

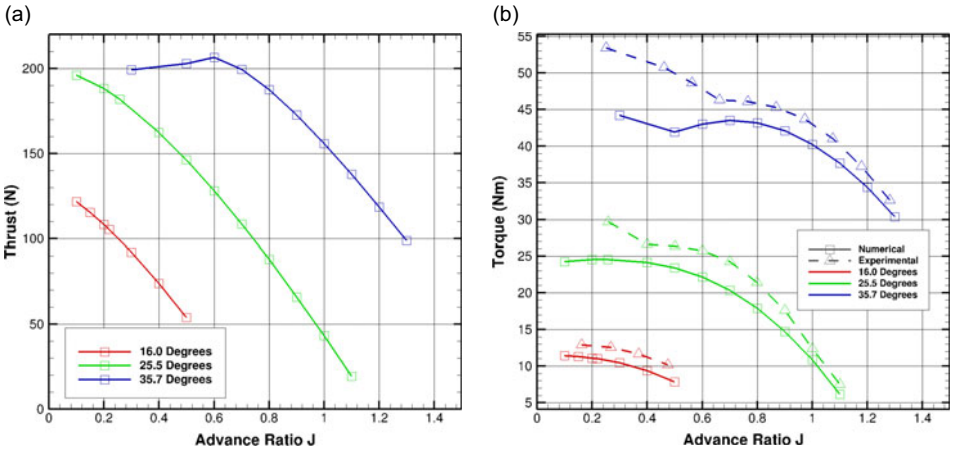

Thrust. Torque.

Figure 8. *Thrust obtained from simulations and comparison between estimated torque and recent wind tunnel experiments performed by Croke et al. [12]. MENtOR blade, 1080RPM, pitch angles of 16, 25.5 and 35.7 degrees.*

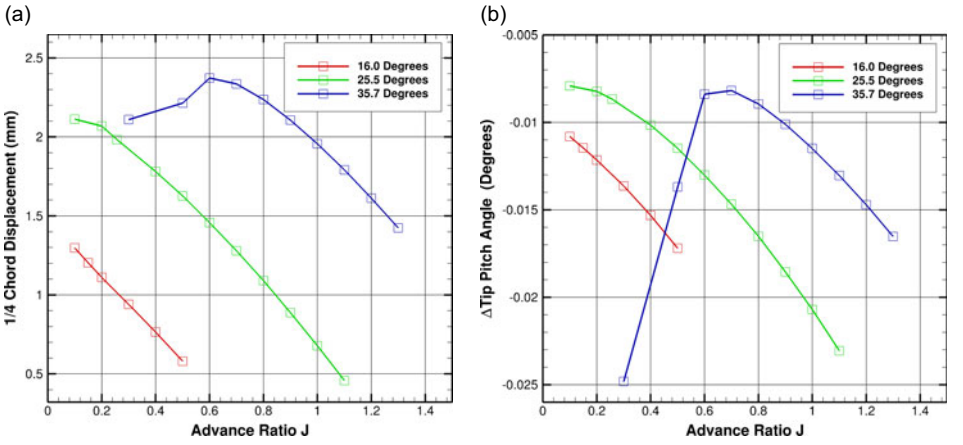

Quarter chord tip displacement. Change in blade tip pitch angle from rigid to deformed.

Figure 9. *Static aeroelastic tip displacements. MENtOR blade, 1080RPM, pitch angles of 16, 25.5 and 35.7 degrees.*

for most modes. However, it can be observed that the fluctuations are larger as the pitch angle increases. The higher order modes were found to have a very small contribution to the computed deformed shape.

Similar observations can be made for the modal forces. The unsteadiness of the flow is evident from the fluctuations of the forces. As the blade pitch angle increases, the fluctuations also increase and the deformations also tend to increase. The softer blade and the baseline blade, at 35.6 degrees pitch, have projected forces of similar magnitudes and fluctuations. Overall, each mode is aperiodic, and there is also some frequency beating, particularly in the 5^{th} mode. This is shown in Fig. 11(d), where the baseline blade repeatedly shows quiescent periods, followed by larger amplitude activity.

https://doi.org/10.1017/aer.2025.10060 Published online by Cambridge University Press

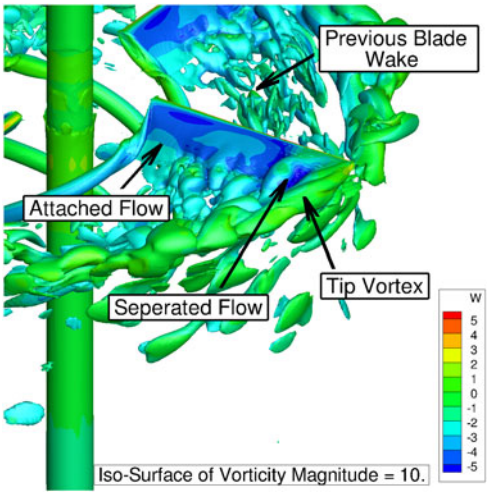

Figure 10. *Instantaneous view of the flow around the MENtOR blade, 3000 RPM, advance ratio J=0.3, pitch angles of 35.6 degrees at 75%R, time-marching simulation.*

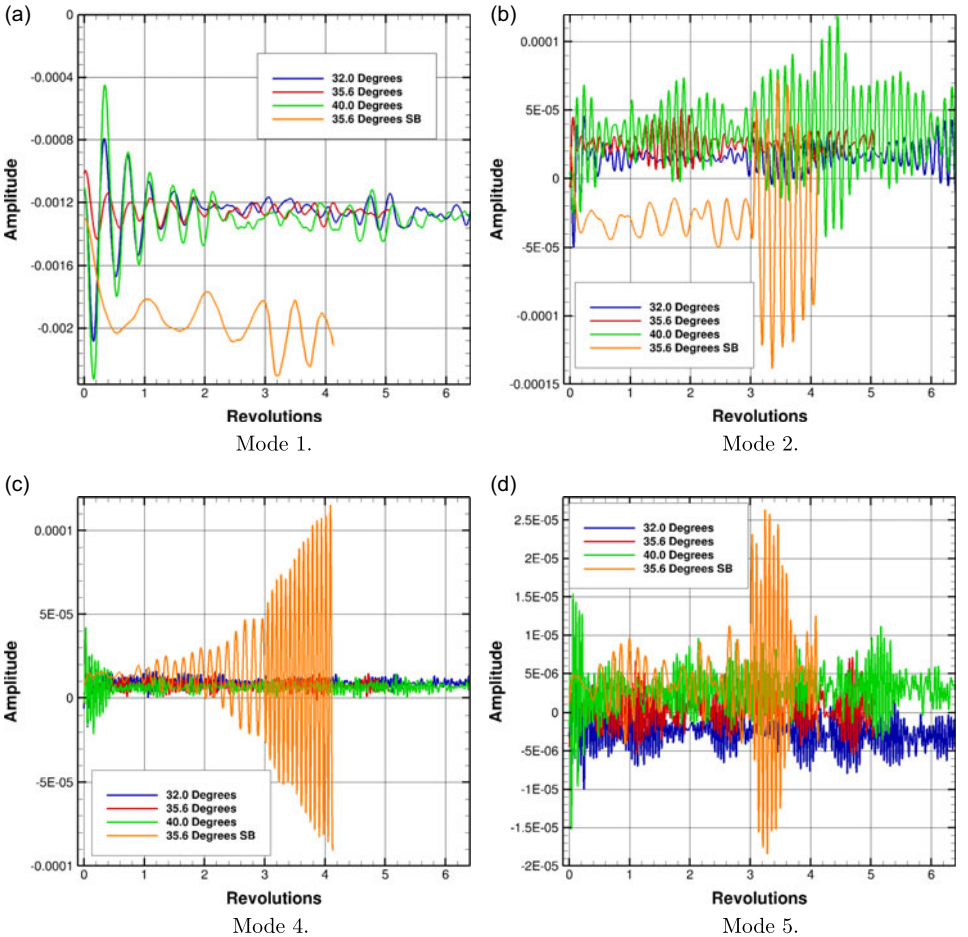

Mode 1. Mode 2.

Mode 4. Mode 5.

Figure 11. *Time history of modal amplitudes. MENtOR blade, 3000 RPM.*

https://doi.org/10.1017/aer.2025.10060 Published online by Cambridge University Press

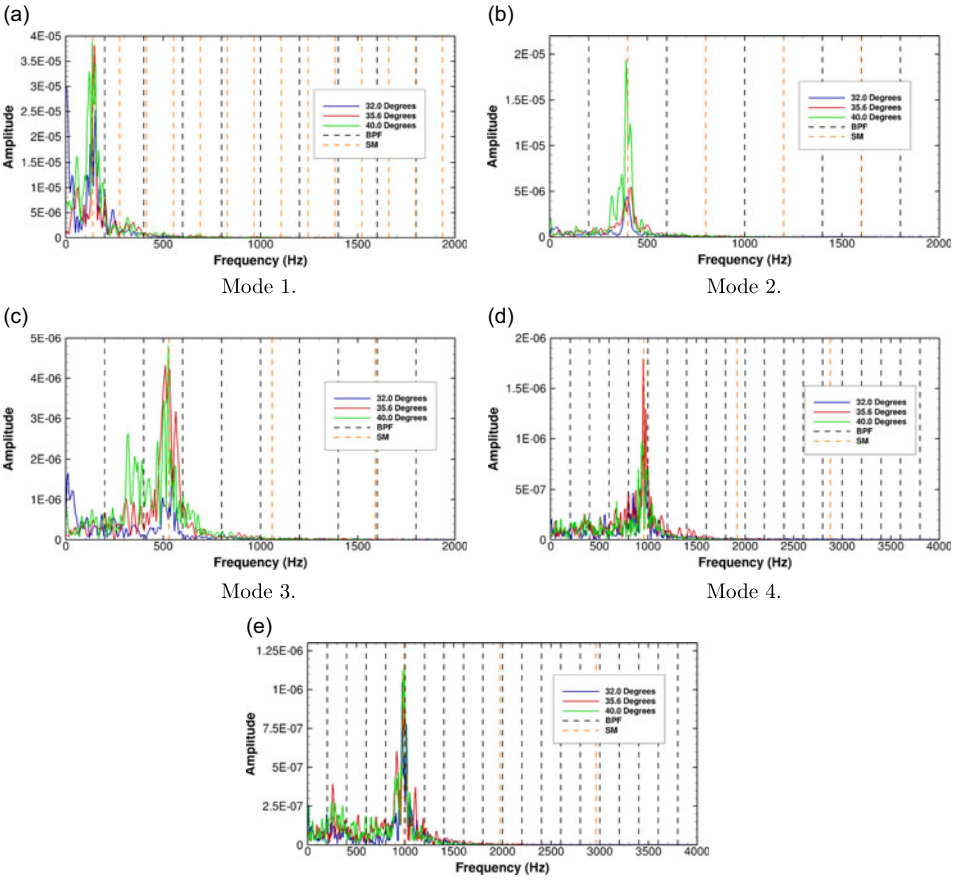

Figure 12. *Frequency content of modal amplitudes for the MENtOR blade. Black dashed lines are the BPF and their harmonics, orange dashed lines are the eigen-modes and their harmonics, 3000 RPM, advance ratio J=0.3, pitch angles of 32, 35.6 and 40 degrees at 75%R.*

3.3 Frequency analyses

To observe the frequencies of the modal deformations and forces, Fourier transforms were conducted. Firstly, the mean values are removed from each of the signals. The signals were also processed using a Hanning [34] windowing method, and zero damping was applied before the Fourier transform was computed. The spectra of the baseline blades can be seen in Figs 12 and 13 for the modal amplitudes and forces, respectively. The black dashed lines indicate the blade passing frequency and its harmonics. The orange dashed lines indicate the modal frequencies and their harmonics for the 3000 RPM fixed root case. For attached flows, peaks would only occur on the blade passing frequency or on structural modes and their harmonics. Also, there would be minimal broadband content in the signals. Figure 12 shows that the largest amplitudes tend to occur at the frequency for the given structural mode. However, there is significant non-harmonic and broadband content that grows in amplitude as the pitch angle is increased. This increase in broadband amplitude is attributed to the stalled flow and can be observed in the structural deformation. In Fig. 13, it is observed that there are more non-harmonic features, which grow in amplitude as the pitch angle increases. The modal amplitudes and forces for the blade can be found in Figs 14 and 15, respectively. Comparing the modal amplitudes, it is observed that the modal amplitudes are much larger on softer the than that of the baseline blades. This is expected because the modal frequencies of the softer blade are reduced and at the same time a similar forcing will lead to

https://doi.org/10.1017/aer.2025.10060 Published online by Cambridge University Press

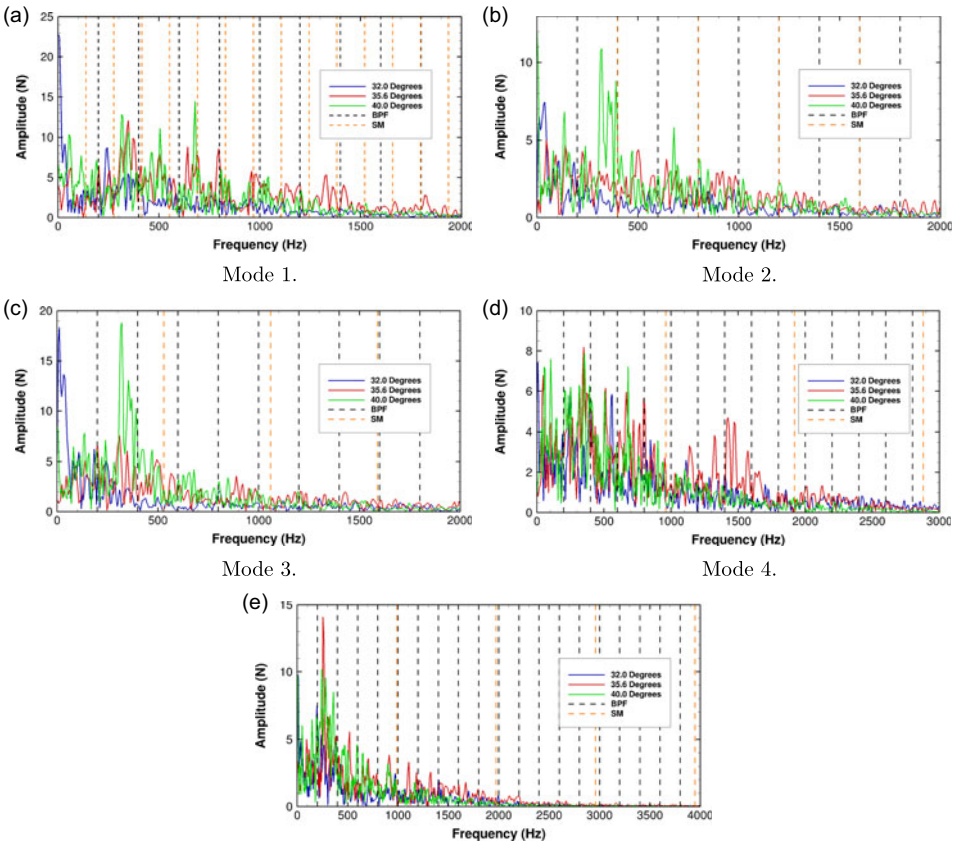

Mode 1. Mode 2.

Mode 3. Mode 4.

Mode 5.

Figure 13. *Frequency content of modal forces for the MENtOR blade. Black dashed lines are the BPF and their harmonics, orange dashed lines are the eigen-modes and their harmonics, 3000 RPM, advance ratio J=0.3, pitch angles of 32, 35.6 and 40 degrees at 75%R.*

larger deformations. Again, the largest amplitudes occur at the modal frequency for each of the modes, and typically are singular sharp peaks. However, for mode 4, a number of large amplitude, non-harmonic frequencies as well as a strong amplitude on the blade passing frequency are observed, unlike the other modes. Figure 15, shows more harmonic content and non-harmonic content where more of the peaks occur on the blade passing frequency or the structural mode and their harmonics.

Figure 16(a and b) presents the deformations for the blade tip, as absolute quarter-chord point displacements and as changes in the local pitch angle for the baseline blades. The quarter-chord is displaced by 8.5mm, 8.7mm and 9.0mm for the 32, 35.6 and 40.0 degree cases, respectively. The minimum to maximum deviations are around 1*mm* for the 32.0 and 35.6 cases and 1.5mm for the 40.0 degree case. The local changes in pitch angle suggest that the propeller deforms dynamically at very high frequencies, but at small magnitudes of 0.05 degrees on average. This small change in pitch angle is not enough for the blade to diverge, and the oscillations are bounded. In Figs 16(c and d) results are shown for the 35.6 degree case with the softer blade. The average displacement magnitude for the quarter chord point on the tip is near 13.5mm with fluctuations of 2mm. The local pitch angle, however, continues to increase over time, showing fluctuations of 3.0 degrees and growing. All of these cases demonstrate stall flutter where the unsteady stalled loads induce fluctuations in the structural deformation. One thing to consider is that as the deformations grow, it becomes more challenging to generate high quality grids as the cell skewness can deteriorate with more deformation.

https://doi.org/10.1017/aer.2025.10060 Published online by Cambridge University Press

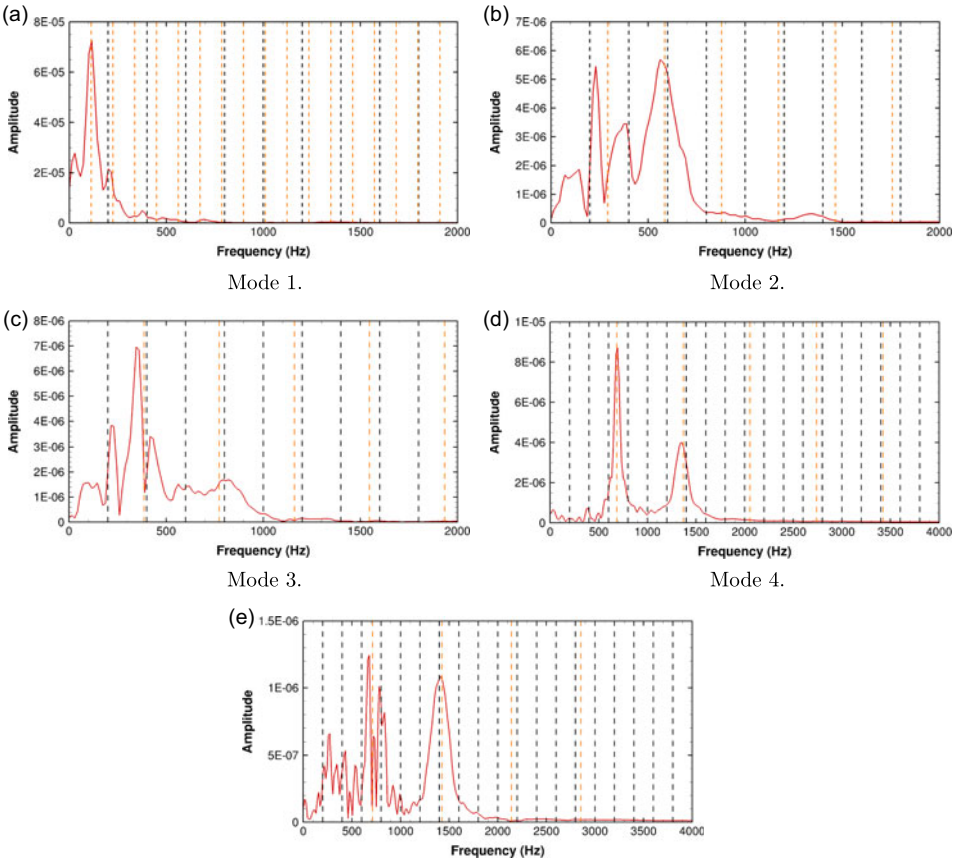

Figure 14. *Frequency content of modal amplitudes for the softened MENtOR blade. Black dashed lines are the BPF and their harmonics, orange dashed lines are the eigen-modes and their harmonics, 3000 RPM, advance ratio J=0.3, pitch angle of 35.6 degrees at 75%R.*

3.4 Analyses of flow probes

To investigate the non-harmonic flow content of the stalled flow and its relationship to the structure, a grid of probes were placed in the flow domain. These probes can extract all flow quantities. However, in this case we used the pressure. The probes were positioned as shown in Fig. 17. They were equally spaced and numbered with grid indexing as: $(i + nx \times j + ny \times nx \times k)$. The probe positions are considered with respect to the locations of the anti-nodes. The first bending mode peaks near probe 32, as shown in Fig. 17(a). The probe is also away from the tip vortex. Comparisons are shown for the softer blade as the larger deformations make it easier to find the frequencies in the probes. The comparison of modal amplitude for the first mode and the frequency content of pressure at probe 32 is shown in Fig. 18. The first non-harmonic frequency, around 20Hz, is seen in both the probe signal and in the modal amplitude of mode 1. The first BPF is also matched for both probe and modal amplitude. However, there were frequencies in the probe signal that were not found in the modal amplitude of the first mode.

For this, we need to consider other modes, as identified and shown in Fig. 19. Modes 3, 4 and 5 have large mode shape deformations near the same location. The comparison is shown in Fig. 20. In these modes, the frequencies for the harmonic and non-harmonic features are matched. This suggests that the non-harmonic features are driving the deformation of the blade structure. To further explore this,

https://doi.org/10.1017/aer.2025.10060 Published online by Cambridge University Press

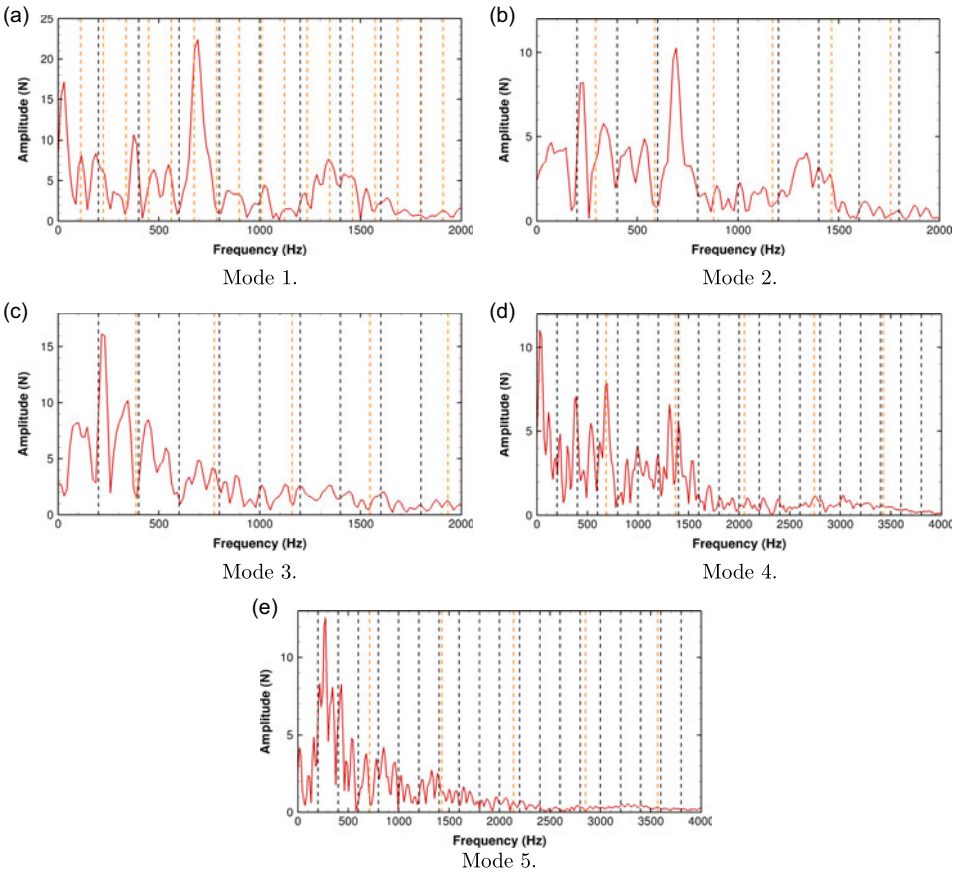

Mode 1. Mode 2.

Mode 3. Mode 4.

Mode 5.

Figure 15. *Frequency content of modal forces for the softened MENtOR blade. Black dashed lines are the BPF and their harmonics, orange dashed lines are the eigen-modes and their harmonics, 3000 RPM, advance ratio J=0.3, pitch angle of 35.6 degrees at 75%R.*

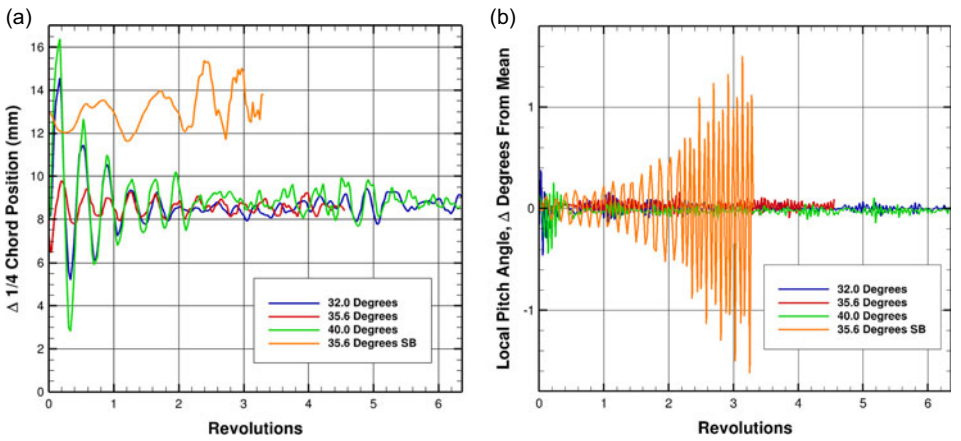

Quarter chord tip displacement. Change in tip pitch angle.

Figure 16. *Tip deflections and twist for the MENtOR blade, 3000 RPM, advance ratio J=0.3, pitch angles of 32, 35.6 (baseline and softened blade) and 40.0 degrees at 75%R.*

https://doi.org/10.1017/aer.2025.10060 Published online by Cambridge University Press

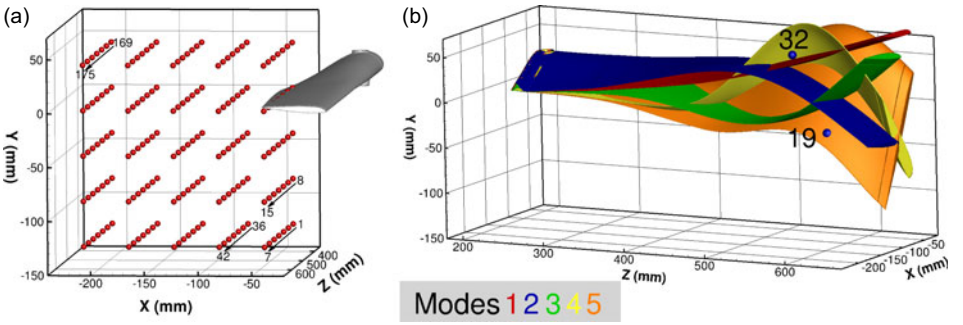

Probe numbering scheme. Probe 19 and 32 with respect to first five mode shapes.

Figure 17. *Probe numbering scheme and probes 19 and 32 with respect to first five mode shapes of the blade.*

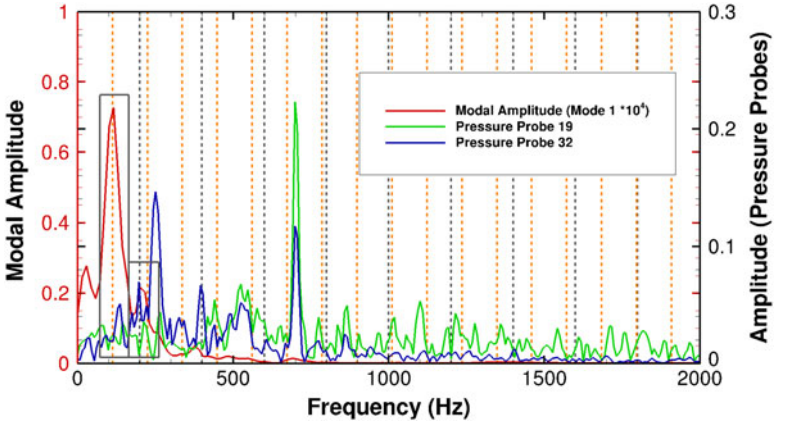

Figure 18. *Comparison of the frequencies and peak amplitudes of mode 1 with scaled pressure data of probes 19 and 32, softer blade, 35.6 degrees.*

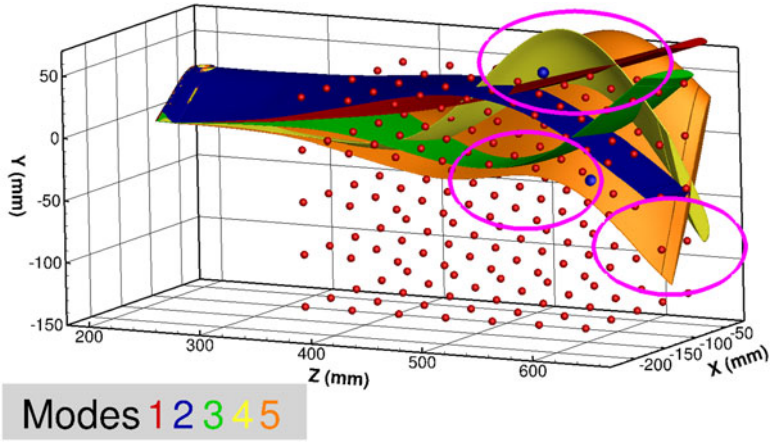

Figure 19. *Probe positions and visualisation of the first five mode shapes of the blade. Magenta ellipses show examples of regions with grouped anti-nodes.*

https://doi.org/10.1017/aer.2025.10060 Published online by Cambridge University Press

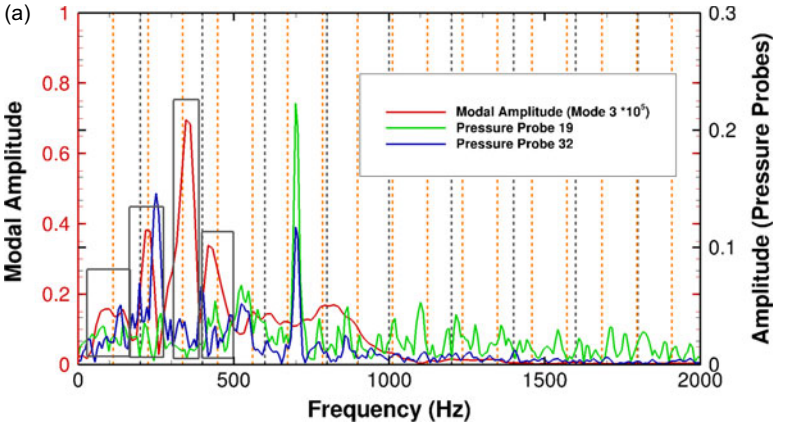

Mode 3.

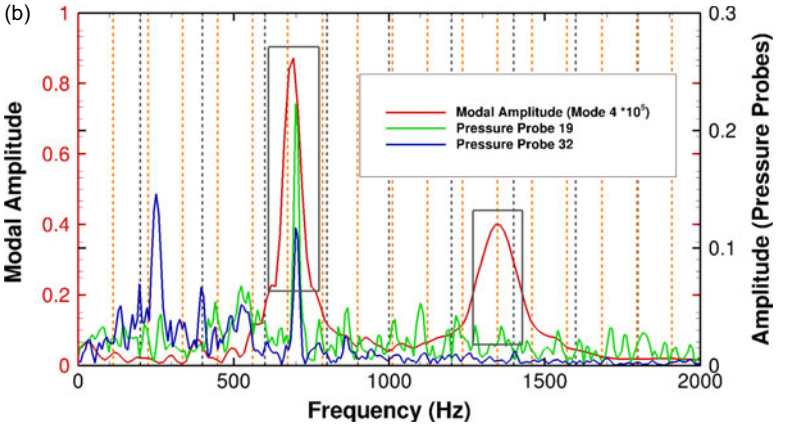

Mode 4.

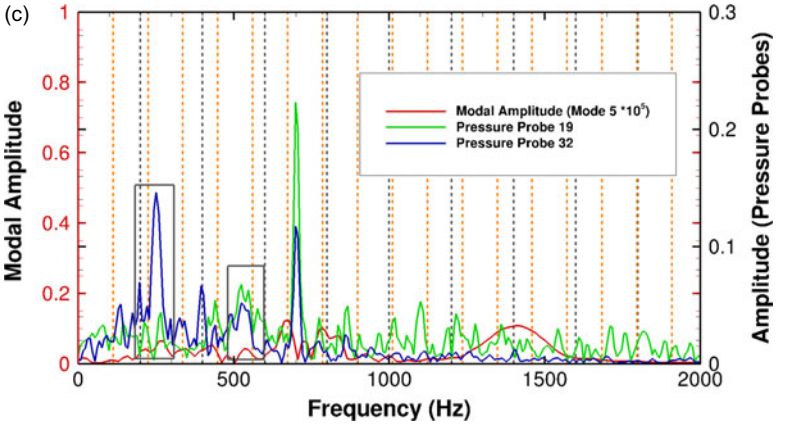

Mode 5.

Figure 20. *Comparison of the frequencies and peak amplitudes of modes 3 and 5 with scaled pressure data of probes 19 and 32, 35.6 degree, baseline blade.*

https://doi.org/10.1017/aer.2025.10060 Published online by Cambridge University Press

Probe 19, also shown in Fig. 17 was considered. This probe is below and behind the blade which places it into a more turbulent region of the flow. In Figs 18 and 20, it can be observed that there is more broadband content due to the growth of turbulence in that region. However, the major harmonic and non-harmonic content in the flow is clearly present. Comparing probe 19 with probe 32 larger modal amplitudes in probe 19 are seen in the torsional content. However, not all of mode 1, non-harmonic peaks are found in probe 19, compared to probe 32. This is due to where the probes are located, regarding proximity with the anti-nodes of the mode shapes. For a given mode shape, if a probe is located in an area where there are large modal deformations then it is expected that that frequencies of that modal amplitude will have similar frequency content to the probe. The opposite of which is also true. However, there are regions where multiple modes show large deformations, in these cases the pressure probes contain the frequencies of several modes, and the deformations receives inputs from several modes amplitude will primarily reflect the frequency of its respective mode. In Fig. 19, the magenta ellipses show some regions where the modal deformations are overlapped across multiple modes.

4.0 Conclusions and future work

This paper presented results for numerical simulation of propeller fluid/structure interactions, pertinent to stall flutter. An in-house Navier-Stokes method was used and the structural representation of the blades was via 3D FE models. The models were used for extracting the normal modes of the blades, and modal-based time-marching simulations were conducted. A small number of quasi-steady simulations were also performed to allow for comparisons with available experimental data, at pre-stall conditions, where the flow is steady.

For the investigated cases and propellers, the simulation results provided good estimates for the necessary power. Given the uncertainties in experiments and CFD simulations, the agreement was seen as adequate and provided confidence in the obtained results for the deformations and vibrations of the blades. The main set of results was for stalled cases, simulated using dynamic fluid/structure interaction. The results showed that the stalled flow resulted in increased vibration of the blades compared to attached flow cases. As stall progressed, larger amplitudes of oscillations in bending and torsion with a beating effect were seen on the results. This is due to the nature of the stalled flow with periods of re-attaching and periods of vortex shedding. Softening the blade structure provided larger deformations, and the blade was diverging in torsion. The rest of the cases showed bounded oscillations, indicative of onset of stall flutter. Unfortunately the flutter conditions were outside the range of safe operation of the wind tunnel used for providing the validation data of section 2.3.1.

The stall flutter phenomenon was driven by the flow as the probe analyses showed. Interestingly, probes close to anti-nodes for different modes showed significant non-harmonic unsteady content. Again, this is expected in stall flutter. The frequencies correspond to the structural modes. However the amplitude depends on the forcing generated by the unsteady flow.

The current research highlights the potential of modern CFD and fluid/structure interaction methods and sets requirements for future investigations and experiments. These include the measurement of time-resolved velocities in the flow and their correlation with on-blade time-resolved strain gauges. Pressure measurements on the blade are also highly desirable. This research is now directed towards analysing different blade designs made to stall at milder flow conditions in order to make tests easier and provide more data for validation.

Acknowledgments. The support of DOWTY propellers via the NESPA project is gratefully appreciated.

References

[1] Fung, Y., *An Introduction to the Theory of Aeroelasticity*, Dover Publications, 3rd ed., 1993.
[2] Higgins R., *A review of propeller stall flutter*, Ph.D. thesis, University of Glasgow, 2020.
[3] Delamore-Sutcliffe D.W. and Greenwell D.I., "A model for the fast prediction of propeller stall flutter," *25th AIAA Applied Aerodynamics Conference*, 2006, doi: 10.2514/6.2006-3477
[4] J.E., B., "The effects of various parameters, including Mach number, on propeller-blade flutter with emphasis on stall flutter," Tech. rep., National Advisory Commitee for Aeronautics, 1955.

https://doi.org/10.1017/aer.2025.10060 Published online by Cambridge University Press

[5] Higgins R., Barakos G.N., and Filippone A., "A review of propeller stall flutter," *Aeronaut. J.*, 2022, **126**, pp 1678–1717.
[6] A.F., S., "Analysis and Test Evaluation of the Dynamic Stability of Three Advanced Turboprop Models at Zero Forward Speeds," Contractor Report 175025, National Aeronautics and Space Administration, 1985.
[7] A.F., S., "Analysis and Test Evaluation of the Dynamic Response and Stability of Three Advanced Turboprop Models at Low Forward Speeds," *Contractor Report 175026*, National Aeronautics and Space Administration, 1985.
[8] Kaza K., Mehmed O., Williams M., and MOSS L., "Analytical and experimental investigation of mistuning in propfan flutter," *28th Structures, Structural Dynamics and Materials Conference*, 1987, p. 739.
[9] O., M., "Propfan model wind tunnel aeroelastic research results," *NASA, Lewis Research Center, Lewis Structures Technology, 1988. Volume 1: Structural Dynamics*, 1988.
[10] Armstrong, R., Pucher, M., Williams, W., Watts, R., Jones, L., and Gibson, S., "Straingauge Test Report on a Spin Test Carried out on a Typc (c) R.305/3-82-F/6 Propeller on the Spinning Tower at the R.A.E. Farnborough, Hants". Tech. Rep. 093.1.592, DOWTY Propellers, 1979.
[11] Zagaglia D., Croke A., Green R.B., and Barakos G.N., "Development of the UK National Rotor Rig For Aeroelastic Testing of Rotary Wings," *49th European Rotorcraft Forum (ERF 2023)*, Germany, 2023.
[12] Croke A., Zagaglia, D., Woodgate M.A., Green R.B., and Barakos G.N., "Experimental Investigation into the Onset of Stall Flutter on Tiltrotor Blades," *49th European Rotorcraft Forum (ERF 2023)*, Germany, 2023.
[13] Croke A.D., Zagaglia D., McKechnie M., Green R.B., and Barakos G.N., "Experimental investigation into the onset of stall on tiltrotor blades in propeller mode," *CEAS Aeronautical Journal*, 2025, pp. 1–15.
[14] Steijl R., Barakos G.N., and Badcock K., "A framework for CFD analysis of helicopter rotors in hover and forward flight," *Int. J. Numer. Method. Fluid.*, 2006, **51**, 819–847, doi: 10.1002/d.1086
[15] Steijl R. and Barakos G.N., "Sliding mesh algorithm for CFD analysis of helicopter rotor-fuselage aerodynamics," *Int. J. Num. Method. Fluid.*, 2008, **58**, 527–549, doi: 10.1002/d.1757
[16] Barakos G.N. and Johnson C., "Acoustic comparison of propellers," *Int. J. Aeroacoustics*, 2016, **15**, 575–594, doi: 10.1177/1475472X16659214
[17] Higgins R.J., Zarev A., Barakos G.N., and Green R.B., "Numerical Investigation of a Two-Bladed Propeller Inflow at Yaw," *J. Aircr.*, 2020, **57**, doi: 10.2514/1.C035647
[18] Scrase N. and Maina M., "The Evaluation of Propeller Aero-acoustic Design Methods by Means of Scaled-Model Testing Employing Pressure Tapped Blades and Spinner," *International Council of the Aeronautical Sciences*, California, USA, 1994.
[19] Gomariz-Sancha A., Maina M., and Peace A.J., "Analysis of propeller-airframe interaction effects through a combined numerical simulation and wind-tunnel testing approach," *53rd AIAA Aerospace Sciences Meeting*, Kissimmee, Florida, USA, 2015.
[20] Knepper A. and Bown N., "IMPACTA Wind-tunnel Instrumentation Specification," *Dowty Propellers (GE Aviation Systems Ltd)*, 2014, ITS 01777, Issue 3.
[21] Zarev A. and Green R.B., "Experimental investigation of the effect of yaw angle on the inflow of a two-bladed propeller," *Aerosp. Sci. Technol.*, 2020, **103**.
[22] Osher S. and Chakravarthy S., "Upwind schemes and boundary conditions with applications to Euler equations in general geometries," *J. Comput. Phys.*, 1983, **50**, 447–481, doi: 10.1016/0021-9991(83)90106-7
[23] van Leer B., "Towards the ultimate conservative difference scheme. V.A second-order sequel to Godunov's Method," *J. Comput. Phys.*, 1979, **32**, 101–136, doI: 10.1016/0021-9991(79)90145-1
[24] Jameson A., "Time-Dependent Calculations Using Multigrid, with Applications to Unsteady Flows past Airfoils and Wings," *AIAA 10th Computational Fluid Dynamics Conference*, 1991.
[25] Axelsson O., *Iterative Solution Methods*, Cambridge University Press: Cambridge, MA, 1994, doi: 10.1017/CBO9780511624100
[26] Babu S.V., Loupy G.J.M., Dehaeze F., Barakos G.N., and Taylor N.J., "Aeroelastic simulations of stores in weapon bays using Detached-Eddy Simulation," *J. Fluid. Struct.*, 2016, **66**, 207–228, doi: 10.1016/j.jfluidstructs.2016.07.014
[27] MSC Software, *MSC.Nastran 2004*, 2003.
[28] Rapaport D.C., *The Art of Molecular Dynamics Simulation*, Cambridge University Press, 2nd ed., 2004, doi: 10.1017/CBO9780511816581
[29] Beeman D., "Some multistep methods for use in molecular dynamics calculations," *J Comput. Phys.*, 1976, **20** (2), doi: 10.1016/0021-9991(76)90059-0
[30] Shepard D., "A Two-dimensional Interpolation Function for Irregularly-spaced Data," *Proceedings of the 1968 23rd ACM National Conference*, New York, NY, USA, 1968.
[31] Biava M. and Barakos G.N., "Optimisation of Ducted Propellers for Hybrid Air Vehicles Using High-Fidelity CFD," *Aeronaut. J.*, 2016, **120** (1232), 1632–1657, doi: 10.1017/aer.2016.78
[32] Renka R.J., "Multivariate Interpolation of Large Sets of Scattered Data," *ACM Trans. Math. Softw.*, 1988, 139–148, doi: 10.1145/45054.45055
[33] "MENtOR Project Homepage," https://www.gla.ac.uk/research/az/mentor/ (accessed 30 October 2024).
[34] Essenwanger O.M., *General Climatology: 2*, No. v. 1-2 in World survey of climatology, Elsevier, 1986.

Cite this article: McKechnie M. and Barakos G. Aeroelastic analysis of propeller blades at stall flutter onset. *The Aeronautical Journal*, https://doi.org/10.1017/aer.2025.10060